EECoG-Comp: An Open Source Platform for Concurrent EEG/ECoG Comparisons: applications to connectivity stuides

Qing Wang[1] · Pedro Antonio Valdés-Hernández[2] ·Deirel Paz-Linares[1]·Jorge Bosch-Bayard[3] · Naoya Oosugi[4] · Misako Komatsu[5] · Naotaka Fujii[4] · Pedro Antonio Valdés-Sosa[1, 6, *]

1. The Clinical Hospital of Chengdu Brain Science Institute, MOE Key Lab for Neuroinformation, University of Electronic Science and Technology of China, Chengdu, China;
2. Department of Biomedical Engineering, Florida International University, Miami, FL, United States;
3. Unity of Neurodevelopment, Institute of Neurobiology, UNAM, Campus Juriquilla, Santiago de Querétaro, Querétaro, México;
4. Laboratory for Adaptive Intelligence, RIKEN Brain Science Institute, Saitama, Japan;
5. Laboratory for Molecular Analysis of Higher Brain Function, RIKEN Center for Brain Science, Saitama, Japan;
6. Cuban Neuro Science Center, La Habana, Cuba.

Abstract

Electrophysiological Source Imaging (ESI) methods are hampered by the lack of "gold standards" for model comparison. Concurrent electroencephalography (EEG) and electrocorticography (ECoG) recordings (namely EECoG) are considered gold standard to validating EEG generative models with primate models have the unique advantages of both flexibility and translational value in human research. However the severe EEG artifacts during such invasive experiments, the complexity of providing sufficiently detailed biophysical models, as well as lacking sound statistical connectivity comparison methods have hampered the availability and analysis of such datasets. In this paper, 1) we provide EECoG-Comp: an open source platform (https://github.com/Vincent-wq/EECoG-Comp) which encompasses the preprocessing, forward modeling, simulation and comparison module; 2) we take the simultaneous EECoG dataset from www.neurotycho.org as an example to illustrate the use of this platform and compare the source connectivity estimation performance of 4 popular ESI methods named MNE, LCMV, eLORETA and SSBL. The conclusion shows the limits of performance of these ESI connectivity estimators using both simulations and real data analysis. In fact, the use of this platform also suggests the need for both improved simultaneous EEG and ECoG experiments and ESI connectivity estimators.

Key words

EEG, ECoG, Forward Modeling, Electrophysiological Source Imaging, Connectivity, Open Science

1. Introduction

Among the non-invasive technologies used to probe normal and pathological brain function in both humans and animals, the Electroencephalography (EEG) (Schomer and Da Silva 2012) is the most affordable, popular and widespread. It also among those with the highest temporal resolution. Alas, like any imaging modality, EEG is not a straightforward and easily invertible proxy of brain activity. In fact, it is a spatially filtered and sub-sampled reflection of hidden brain states, corrupted by noise and artifacts. Indeed at the EEG electrodes, the signal is spatially filtered by volume conduction (van den Broek et al. 1998)—owing to the very low conductivity of the skull—mixing the contribution of the sources of the EEG. It also introduces spurious values of brain coherence, leading to false brain connectivity estimations. For this reason, EEG connectivity should be in principle assessed from the sources, mandating the solution of the inverse problem (Pascual-Marqui 1999) of EEG, i.e. the estimation of brain sources activities from EEG measurements—a technique also called Electrophysiological Source Imaging (ESI).

ESI has been long studied in the attempt to localize epileptic foci (Ding et al. 2007; He et al. 2011). In addition, it has been proposed to study the localization of different brain functions as well as the dynamics of neural connectivity. Nevertheless, ESI methods has important methodological issues and requires external validation or a "gold standard" (Nunez et al. 2019).

1 Qing Wang and Pedro Antonio Valdés-Hernández contributed equally to this paper.

Electrocorticography (ECoG) or intracranial electroencephalography (iEEG) is considered by many as this "gold standard", since it provides more accurate information of the cortical brain states (Nunez et al. 2019). ECoG is a type of invasive monitoring technology with electrodes placed directly on the exposed surface of the cortex to record electrical activity of the brain. ECoG is considered as the "gold standard" for pathological epileptic focus localization (Frauscher et al. 2018). It should be noted that, even though the ECoG electrodes are directly placed on the cortex, the activity at the surface of the cortex is not equivalent to the true "sources" of the "physiological cortical macro columns" proposed by Buxhoeveden et al. (2002), this is the reason why we need to solve the inverse problem for ECoG as well (Nunez et al. 2019).

Solving the inverse problem first requires the solution of the forward problem (Hallez et al. 2007) of EEG and ECoG (EECoG), i.e., the calculation of the so-called lead field matrix (LF)—a mapping matrix from known sources to EECoG measurements—which demands the definition of a head model specifying the spatial distribution of tissue conductivity, a source space model and the location the EECoG electrodes relative to the latter. The more realistic the head model, the more accurate the ESI solutions. Nowadays, high detailed structural Magnetic Resonance Images (MRI) are used to define the head model and either Boundary Element Method (BEM) or Finite Element Method (FEM) are used to calculate the LF. These methods differ in accuracy.

EECoG inverse problem attempts to estimate the "sources" on the basis of the sensor recordings and the LF. Unfortunately, this inverse problem is ill-posed in the Hadamard sense: the null space of the lead field has finite dimension, sabotaging the uniqueness of the solution. Thus, it is necessary to impose priors on the sources such as mimimum energy, sparsity, smoothness and independence; and to restrict the source space with anatomical information, e.g. by forcing the sources to be in the gray matter or by imposing the orientation of the dipoles to be perpendicular to the cortical layer. This is another reason to provide accurate forward head models. Abundant inverse solutions using of these contraints have been developed and implemented, examples being weighted minimum-norm estimation (WMNE) (Hämäläinen et al. 1994), beamforming (BF) (Grech et al. 2008; Van Veen et al. 1997), Blind Source Separation (BSS) (Oosugi et al. 2017), exact Low Resolution Electromagnetic Tomography (eLORETA) (Pascual-Marqui 2007), Sparse Structural Bayesian Learning (SSBL) (Paz-Linares et al. 2017), and so on. This problem is even more difficult for source connectivity estimation, as an aspect that we will pay a close attention.

It follows, due to the complexity of the forward modeling procedure and the uncertainty of the inverse solutions, we can have different source activity and connectivity estimations from different ESI methods. In view of the proliferation of ESI methods. It is quite challenging to determine which is the best and to quantify it reliability. There is general agreement that simulations are not enough to make this decision.

Unfortunately, there is a paucity of data sets that can serve as "gold standards" to evaluate ESI accuracy for real EEG data—unsurprisingly, given the obvious difficulty in having scalp EEG signals in a normal intact head simultaneously with direct brain activity measurements. This was only tackled with few unrealistic though exceptionally useful attempts in the past. That is the case of Leahy et al. (1998) who designed and conducted a multiple dipole phantom consisting of 32 independently programmable and isolated dipoles inserted in a skull mount filled with conductive gelatin. They used this phantom to collect EEG and MEG data to evaluate the performance of current dipole localization methods. In Marin et al. (1998) another realistic conductive skull phantom was used to evaluate the accuracy of forward FEM methods. Later, this phantom was used to evaluate the performance of different ESI methods in Baillet et al. (2001)[2]. Recently, Peterson and Ferris (2018) evaluated the performance of ICA-based connectivity in a phantom in motion. A much more ideal "phantom" to study the effect of the accuracy of ESI methods on assessing brain connectivity and source localization is the one providing scalp EEG signals concurrently with actual and direct whole brain measures of brain activity, such as Local Field Potential (LFP) and Multi-Unit Activity (MUA) (Mattia et al. 2010). However coverage of all brain areas simultaneously with these techniques is imposible. On the other hand, optical imaging (Wang et al. 2003) provides a direct measurement of hemodynamic responses at the cortical level, but all these techniques requires the removal of the skull during the experiment.

[2] Noteworthily, more recent and realistic phantoms, even 3D printed, are now available for these tests (Collier et al., 2012; Li et. Al 2013; Zhang et al. 2013).

A better candidate is the simultaneous EECoG experiment: which measures the brain electrical activity directly over the cortex and obtain simultaneously the scalp EEG after closing the skull. Both can offer comparatively large coverage. However, the invasiveness makes it available only in human clinical and preclinical settings, mainly restricted to pathologies like epilepsy—only targeting the seizure onset zones and thus usually precluding the recording of larger spatial extensions of the cortex (Frauscher et al. 2018).

The same situation is much more advantageous in primate preparations. For example, the Multidimensional Recording (MDR) database (http://neurotycho.org) (Nagasaka et al. 2011) offers such kind of simultaneous EECoG experient data with ECoG covers the left hemisphere of the cortex and EEG covers the whole head. To our knowledge, this is the only open macaque simultaneous EECoG data set currently available. Despite the complexity of the experimental settings, simultaneous EEG and ECoG has the unique advantage of allowing cross validation of two types of recordings originated from the same neural sources. Testing the ESI methods has also been possible with this dataset (Oosugi et al. 2017). Nevertheless, there is still no neuroinformatics platform (pipeline) designed for analyzing and comparing such kind of simultaneous EECoG data, especially for the evaluation of source connectivity estimation.The main reasons are:

1) The artifacts induced by the very complicated primate experimental configurations, which hinders the correct estimation of brain sources activity and connectivity patterns;
2) The difficulty in obtaining a realistic head model that takes into consideration the implanting of very low conductivity ECoG silicone stripes, and the difficulty of giving the lead fields for EEG and ECoG with the same source space;
3) The lack of tools to compare results in terms of connectivity estimation at the same statistical significance.

In this paper, we solve these problems and publicly provide an open source platform named "EECoG-Comp" that has the following features:

1) The customized preprocessing algorithms, including synchronization and model-based artifact removal algorithms;
2) The realistic MRI-based biophysical head model taking in to consideration of the implanted ECoG stripes, and provides FEM-based lead fields for both EEG and ECoG with the same source space;
3) The standard source connectivity simulation and statistical analysis to guarantee the reliability of comparisons.

This platform is shared via https://github.com/Vincent-wq/EECoG-Comp, and the data will be available upon request. For a detailed description of the content shared, refer to Table 2 in next section. Our platform and results have been used in the research of estimating and evaluate directed connectivity (Papadopoulou et al. 2015) and testing the resolution properties of different inverse solutions (Todaro et al. 2018). We expect this platform to be used by the developers of ESI methods.

In this paper, we describe the simultaneous EECoG platform in section 2. As an illustration of the usefulness of this platform, we take ESI methods connectivity comparison as an example in section 3 and 4. Our preliminary results yield interesting and cautionary results, the performance of the tested ESI methods varies when the source connectivity is different in both simulation and real data, and all of the tested methods do not improve much accuracy (less than 10%) compared with direct connectivity estimation from the source activities. The results from the illustration of this platform remind us that we should be more careful when interpreting the estimated "source connectivity" from ESI methods. These results can also provide us useful information in planning future experiments to improve ESI methods.

2. Concurrent EEG/ECoG Comparison Open Source Platform

The concurrent EEG/ECoG comparison open source platform (**EECoG-Comp**) is composed of four main modules as depicted in Fig. 1, and they are: 1) **EECoG_Preproc** (Fig. 1 upper right) for preprocessing, 2) **EECoG_FWM** (Fig. 1 lower left) for realistic forward modeling, 3) **EECoG_scSim** (Fig. 1 upper left) for EECoG source connectivity simulation, and 4) **EECoG_conComp** (Fig. 1 lower right) for inverse solution, graph model estimation and statistical comparison. They aim to, respectively, 1) reject the artifacts induced by the very complicated

experimental configurations, 2) solve the EEG forward problem in presence of the very thin silicone ECoG subdural array, 3) create simulations as null model for the testing of methods (for example ESI methods) to make sure that the methods are at least reliable in simulations, 4) solve the inverse problem, estimate and compare the source level connectivity of EECoG at the same significance level.

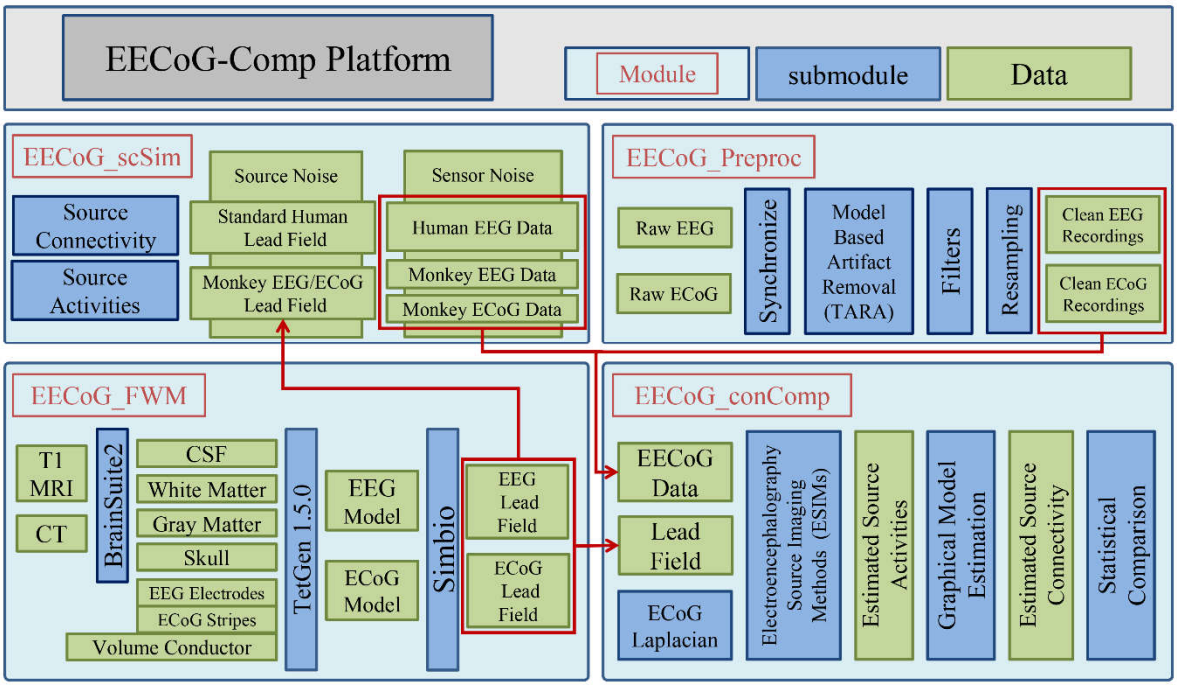

Fig. 1 System diagram for the open source EECoG-Comp platform.

In what follows, we describe the modules and submodules relevant to specific challenges that are identified as essential to EECoG connectivity analyses. We take the simultaneous EECoG experiment from neurotycho.org (http://neurotycho.org/eeg-and-ecog-simultaneous-recording) as an example to illustrate how EECoG-Comp is working in the following subsections, and use the following mathematical notations to better explain the theory and methods bebind all the modules: $x \in \mathbb{R}$ (lower case, Italian, not bold) is a function or a variable, $\boldsymbol{x} \in \mathbb{R}^N$ (lower case, Italian, and bold) is a vector, $\boldsymbol{X} \in \mathbb{R}^{M \times N}$ (upper case, Italian, and bold) is a matrix or matrix operator, please refer to the table of Appendix 1 for the full notations.

1 MDR Recording

This dataset is partly described in Nagasaka et al. (2011) and Oosugi et al. (2017). All the experimental and surgical procedures were performed in accordance with protocols approved by the RIKEN ethical committee (No. H22-2-202(4)) and the recommendations of the Weatherall report, "the use of non-human primates in research". During the experiment, a macaque monkey (*macaca fuscata*) was seated in a primate chair with hands tied and head movement restricted. The eyes of the monkey were covered to avoid evoked visual responses during the entire experimental period.

The electrophysiological data (EEG and ECoG) was recorded during two conditions: 1) awake resting state with eyes folded and movements restricted; and 2) drug induced anesthesia: 1.15 ml (8.8 mg/Kg) ketamine hydrochloride and 0.35 ml (0.05 mg/Kg) medetomidine injection. For each condition, two five-minute trials of simultaneous resting state EEG and ECoG activities were recorded.

For ECoG, the skin, skull and dura of the monkey's left hemisphere was carefully removed. Then, a modified human subdural ECoG array, adapted to the monkey physiology (Nagasaka et al. 2011), was inserted in the subdural space between the arachnoid membrane and the dura mater (see Fig. 2). This array consisted in a set of 1 mm-thick silicone stripes containing and insulating 128 ECoG platinum disk-shaped electrodes 3 mm in diameter, leaving only a hole in the silicone of 0.8 mm diameter at the center of each electrode. The electrodes, with a separation of 5 mm between each other, covered the frontal, parietal, temporal and occipital lobes and part of the medial wall of the left cortex, as depicted in the X-ray image in . The X-ray images were obtained by using the VPX-30E system (Toshiba Medical Supply, Tokyo, Japan) with 8.0 mA in current and 90 kV in voltage. The reference electrode were rectangular platinum plates in the subdural space between the array and the dura. Another platinum electrode was placed as ground in the epidural space. After placing the ECoG electrodes, the dura, the skull and the skin were carefully placed back (see Fig. 2). ECoG was filtered and recorded by a Cerebus recording system (Blackrock Microsystems, Utah, USA). Plastic connectors from the array to the ECoG system were attached to the top of the head with dental cement and small titanium screws. The sampling rate was 1000 Hz, and the recordings were Butterworth bandpass filtered within 0.3-400 Hz.

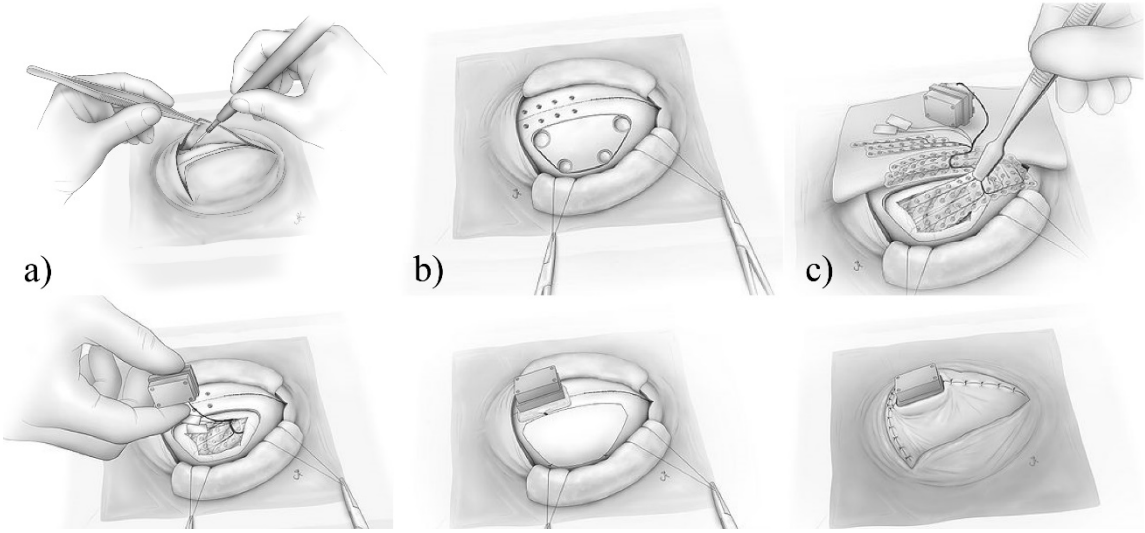

Fig. 2 Illustration of the procedure for implanting ECoG arrays and placing back the dura, the skull and the skin to cover the brain cortical external surface.

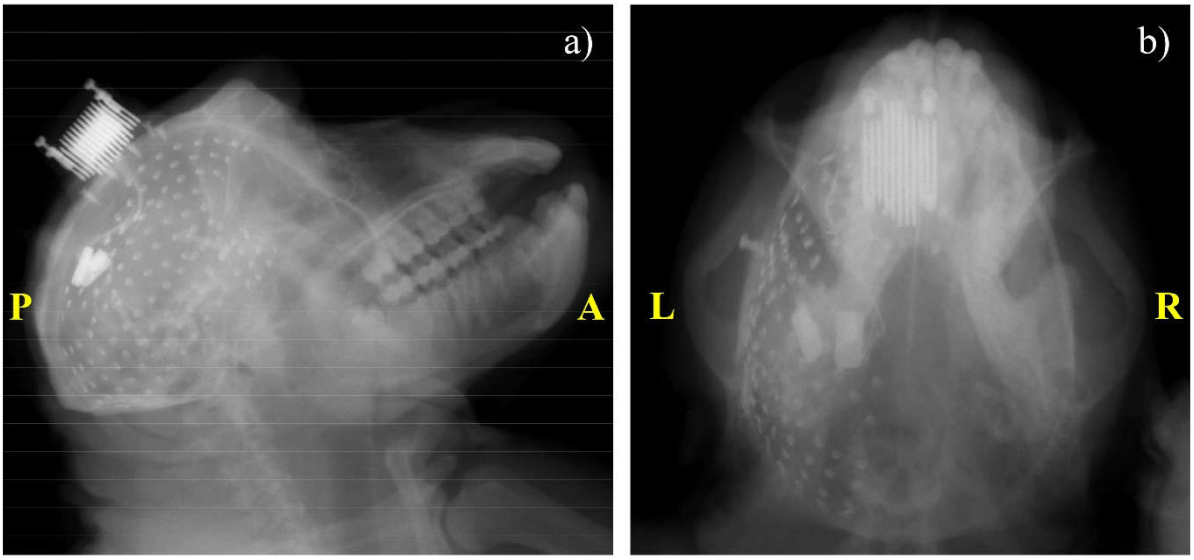

Fig. 3 X-ray images of the ECoG electrodes: 1) sagital view; b) coronal view.

On the other hand, EEG was recorded utilizing a NeuroPRAX system (eldith GmbH, Ilmenau, Germany) with sampling rate of 4096 Hz, using 18 electrodes following the standard 19-electrode 10-20 system; but removing electrode "Cz" to place the ECoG plastic connector. The recordings were down-sampled to 1000 Hz. An external TTL pulse was used to define the beginning and the end of the EEG and ECoG recordings interval of interest, for

synchronization. We will illustrate how this platform can help in analyzing the data recorded in such a highly customized experiment with this data set.

2 Preprocessing module: EECoG_Preproc

The first challenge of analyzing the EECoG (MDR) data is the high level of artifacts present in the recordings. We therefore addressed this attention to assimilating procedures to alleviate this interference.

The first step of preprocess the simultaneous EECoG recordings is synchronization, and we synchronized the original 4096 Hz EEG and 1000 Hz ECoG recordings with the provided "Trigger" signal. After that, the "Trigger" channels are removed from both recordings. Then, we average referenced them. Based on the artifact properties of sparse spikes and step-like discontinuities of the EEG data, we further use Transient Artifact Reduction Algorithm (TARA, the theory will be detailed latter) (Selesnick et al. 2014) to clean these artifacts, the results are shown in Fig. 4 below. After the above procedures, we use the notch filter to remove the power-line artifact of 50 Hz and applied the Butterworth high-pass filter of 0.3 Hz. At last, we down-sampled the EECoG recordings to 400 Hz and bandpass to alpha band (8 Hz to 12 Hz) for latter analysis. It is to be noted that we did not observe a clear alpha peak, even not from the occipital recordings of both EEG and ECoG despite our careful artifact rejection and pre-processing. This platform also supports FieldTrip (Oostenveld et al. 2011) and EEGLab (Delorme and Scott 2004) data structure.

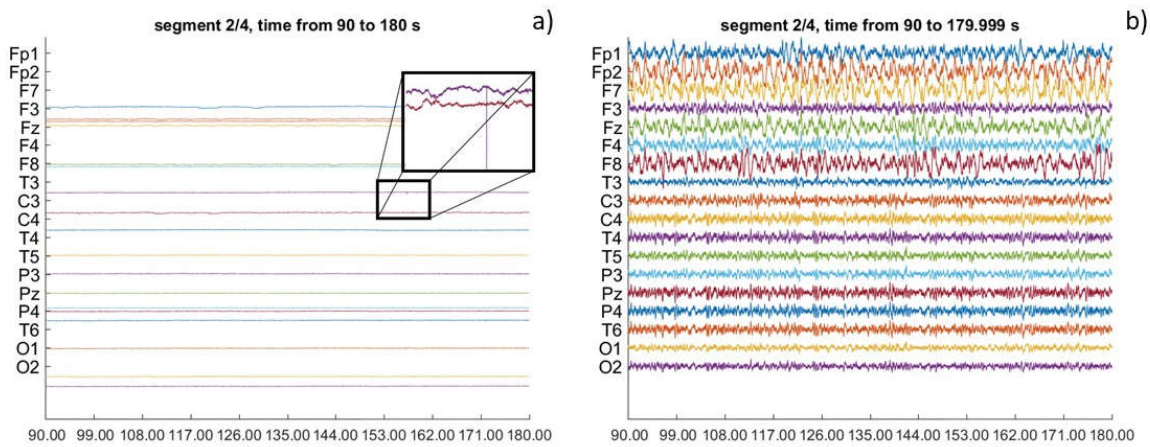

Fig. 4 The comparison of the EEG recordings before and after preprocessing with TARA. (a) The original EEG recordings of anesthesia trial 5 (Y scale is [-2909.6, 2690.4] unit), the zoomed in window shows the artifacts of sparse spikes and step-like discontinuities in the original recordings. (b) The cleaned EEG recordings of anesthesia trial 5 (Y scale is [-60, 60] unit).

Here, we give further brief introduction to the theory behind TARA (Selesnick et al. 2014). The two types of artifacts that TARA is aiming to remove are: sparse spikes (sparse functions) and step-like discontinuities (functions with sparse first derivatives), and the model (for one channel) can be written as:

$$\boldsymbol{v}_{ob} = \boldsymbol{v}_c + \boldsymbol{a}_1 + \boldsymbol{a}_2 + \boldsymbol{\mu}, (\boldsymbol{v}_{ob}, \boldsymbol{v}_c, \boldsymbol{a}_1, \boldsymbol{a}_2, \boldsymbol{\mu} \in \mathbb{R}^N), \qquad \text{Equation 1}$$

Where $\boldsymbol{v}_{ob}$ is the recorded signal, $\boldsymbol{v}_c$ is the low-pass discrete-time signal (artifact free or clean signal) we aim to obtain. $\boldsymbol{a}_1$ represents the "spare" spike artifacts (type 1), a small number of spikes compared to the length of signal with also small number of nonzero elements in its first derivative. $\boldsymbol{a}_2$ represents the step-like discontinuities (type 2), which also implies a sparse derivative. The term $\boldsymbol{\mu}$ is the additive Gaussian noise. D is the first order differential operator. Based on this, the artifact removal procedure can be formulated into an optimization problem:

$$f_{a_1,a_2}(\lambda_0,\lambda_1,\lambda_2) = \arg\min_{a_1,a_2}\left\{\frac{1}{2}\|B(\boldsymbol{v}_{ob} - \boldsymbol{a}_1 - \boldsymbol{a}_2)\|_2^2 + \lambda_0\sum_n \psi_0([\boldsymbol{a}_1]_n) + \lambda_1\sum_n \psi_1([D\boldsymbol{a}_1]_n) + \lambda_2\sum_n \psi_2([D\boldsymbol{a}_2]_n)\right\},$$

Equation 2

Where λ_i are the regularization parameters, and ψ_i is the penalty function promoting sparsity (or smoothness), which can be $\boldsymbol{l}_1$ or $\boldsymbol{l}_2$ norms (depend on the characteristic of the real data and the assumption of the artifact free signal $\boldsymbol{v}_c$). B denotes the high-pass filter annihilating the low-pass (artifact free) signal $\boldsymbol{v}_c$, and it can be estimated as:

$$\hat{\boldsymbol{v}}_c = A(\boldsymbol{v}_{ob} - \hat{\boldsymbol{a}}_1 - \hat{\boldsymbol{a}}_2) = \boldsymbol{v}_{ob} - \hat{\boldsymbol{a}}_1 - \hat{\boldsymbol{a}}_2 - B(\boldsymbol{v}_{ob} - \hat{\boldsymbol{a}}_1 - \hat{\boldsymbol{a}}_2)\,, \qquad \text{Equation 3}$$

where A is defined as the low-pass filter: $A = \boldsymbol{I} - B$. By introducing TARA, we are able to clean most of the above two types of artifacts as shown in Fig. 4.

After preprocessing, several channels in the EEG (F3, C3, and Fz) and ECoG (channel 38, 50, and 93) have been removed from further analyzing due to bad quality, as visually judged by an expert neurophysiologist.

3 Forward Modeling Module: EECoG_FWM

The second chanllege of simultaneous EECoG data analysis comes from the implanting of the ECoG stripes, which makes the forward modeling procedure much more complex. EEG forward modeling is the first step for Electrophysiological Source Imaging (ESI) analysis, and it can provide the so-called lead field or gain matrix $\boldsymbol{K}$ for further source activity estimation and forward simulation. Thus, EECoG_FWM, as one important module of EECoG-Comp, is created to build the realistic head model for the complex simultaneous EECoG experiment. The EEG forward problem can be formulated as follows:

$$\boldsymbol{V}_{eeg} = \boldsymbol{K}_{eeg}\,\boldsymbol{J} + \boldsymbol{\varepsilon}_{eeg}\,, \qquad \text{Equation 4}$$

While the ECoG forward problem can be writen as:

$$\boldsymbol{V}_{ecog} = \boldsymbol{K}_{ecog}\,\boldsymbol{J} + \boldsymbol{\varepsilon}_{ecog}\,, \qquad \text{Equation 5}$$

where $\boldsymbol{J}$ is the primary current density, $\boldsymbol{V}_{eeg}$ and $\boldsymbol{V}_{ecog}$ are the measured EEG and ECoG signals, $\boldsymbol{K}_{eeg}$ and $\boldsymbol{K}_{ecog}$ are the lead fields for EEG and ECoG, $\boldsymbol{\varepsilon}_{eeg}$ and $\boldsymbol{\varepsilon}_{ecog}$ are the measurement noises for EEG and ECoG, respectively.

The aim of EECoG_FWM module is to estimate $\boldsymbol{K}_{eeg}$ and $\boldsymbol{K}_{ecog}$ from the T1-weigthed Magnetic Resonance Image (MRI) of the subject (in this data set, it is the monkey named Su), these images are used to construct the surfaces (triangular meshes) defining the head model. The T1w image was acquired in a 4T Varian Unity Inova MR scanner (Varian NMR Instruments, Palo Alto, CA) with a 3 in 1 loop surface coil (Takashima Seisakusho Ltd., Tokyo, Japan). The scanning parameters are: TR/TE = 13 ms/3.8 ms, in-plane matrix is $256 \times 256 \times 256$, field of view is $12.8 \times 12.8 \times 12.8\ cm$ with voxel size of $0.5 \times 0.5 \times 0.5\ mm$. This image was segmented into white matter (WM), gray matter (GM) and cerebrospinal fluid (CSF) with BrainSuite2 (Shattuck et al. 2001). The gray and white matter interface surface, as shown in Fig. 5(a), is chosen as the source space model for EECoG, i.e. each of its 104650 nodes can be the location of a current dipole with orientation normal to the surface, and we are using a down-sampled version in latter experiments due to the computational issues. The volume conductor model comprises three compartments 1) WM+GM+CSF, 2) Skull and 3) Skin as shown in Fig. 5(a) with constant conductivities 0.33 S/m, 0.0041 S/m and 0.33 S/m, respectively. These are represented by their boundaries: the “inskull”, the “outstull” and the “scalp”. Additionally, a fourth compartment accounting for the ECoG silicone array was included, with 1 mm thickness and the shape shown in Fig. 5(b), and it is also described in the first subsection named “MDR Recording”. It is very important to account for this compartment because its conductivity is very low and therefore it is determinant on the EEG signals. On the other hand, the EEG electrodes were manually located on the monkey’s scalp using IMAGIC (www.neuronicsa.com) as depicted in Fig. 5(c).

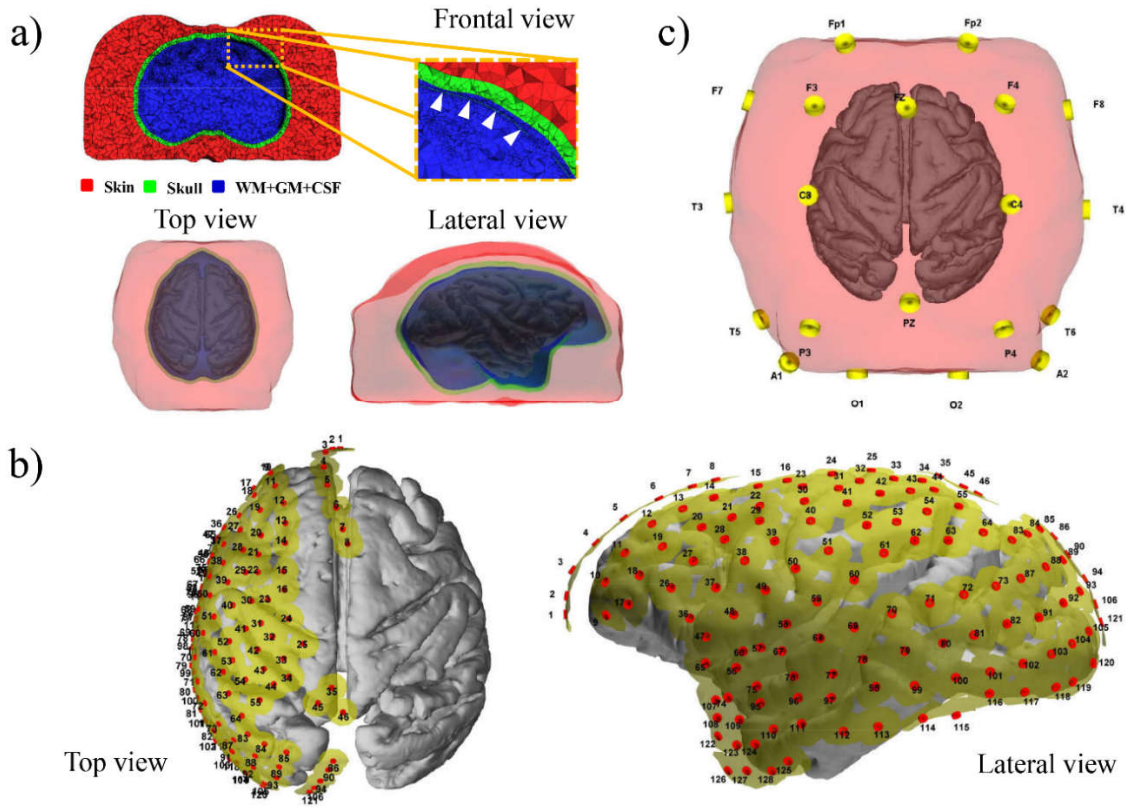

Fig. 5 Head Model of the monkey: a) Tetrahedral meshes defining the source space and the volume conductor model. From inside to outside: source space (cortex), inskull, outskull, and scalp; b) silicone compartment (yellow) and 128 ECoG electrode positions represented (source space is shown as reference); c) The 10-20 system EEG electrodes with the head model.

The tetrahedral meshes in Source Connectivity Comparison Module: EECoG_conComp

Brain connectivity has recieved much attention in recent years (Bassett DS et al. 2017). However, the estimation and comparison of brain connectivity at source level is still very challenging (Zalesky et al. 2010). The next chanllege for EECoG-Comp platform is to compare the source level connectivity with sound statistics. EECoG_conComp is designed to fullfil this goal, and it has the following submodules: 1) ESI methods submodule, which provide the unified interface for all the ESI methods to estimate the source activities; 2) Graphical model estsimation submodule, which estimate the graphical model from the estimated source activities; and 3) The statistical comparison submodule, which compare the estimated graph model parameters at the same statistical significance level. In addition to all these submodules, EECoG_conComp also provides the ECoG Laplacian submodule, which estimates the Laplacian of ECoG over the cortical grid as another way of exploring the "pseudo source connectivity". All these submodules will be detailed below.(a) were created from the surfaces of the head model using TetGen 1.5.0 (Si 2015), an open source software in Linux repositories. During the meshing process the nodes in the source space surface (cortical grid) were forced to be nodes of the tetrahedral mesh to guarantee the Venant's condition. Both EEG and ECoG lead fields were calculated using NeuroFEM. This is a program for computing lead fields using FEM which is part of the SimBio software package (Consortium et al. 2000) (index page: https://www.mrt.uni-jena.de/simbio /index.php/Main_Page). This module can provide average referenced LFs with 3d cortical grid.

It should be noted that only 15 channels of EEG left after removing the bad channels, and 125 channels of ECoG left. Finally, we only take the left hemisphere of the cortical grid (source space) and study its connectivity due to the the limited coverage of ECoG in real data analysis.

4 Source Connectivity Comparison Module: EECoG_conComp

Brain connectivity has recieved much attention in recent years (Bassett DS et al. 2017). However, the estimation and comparison of brain connectivity at source level is still very challenging (Zalesky et al. 2010). The next chanllege for EECoG-Comp platform is to compare the source level connectivity with sound statistics. EECoG_conComp is designed to fullfil this goal, and it has the following submodules: 1) ESI methods submodule, which provide the unified interface for all the ESI methods to estimate the source activities; 2) Graphical model estsimation submodule, which estimate the graphical model from the estimated source activities; and 3) The statistical comparison submodule, which compare the estimated graph model parameters at the same statistical significance level. In addition to all these submodules, EECoG_conComp also provides the ECoG Laplacian submodule, which estimates the Laplacian of ECoG over the cortical grid as another way of exploring the "pseudo source connectivity". All these submodules will be detailed below.

ECoG Laplacian Submodule

With its wide acceptance, we shall use the ECoG Laplacian over the cortical grid as a surrogate measure to the primary current density $\boldsymbol{J}$. Note that, this estimator is very similar to the "spline Laplacian/dura images" discussed by Nunez and Srinivasan (2006).

The specific challenge of this submodule is to approximate the laplacian over the same cortical grid that will be used for ESI methods with the assumption that, the ECoG Laplacian is smooth over the cortex. Suppose that $\boldsymbol{V}_{cortex}$ is the true voltage on the cortex for our cortical mesh, and the Laplacian on the cortex is $\boldsymbol{\phi}_c$. Thus, we have the voltage on the cortex ($\boldsymbol{V}_{cortex} = \boldsymbol{L}^{-1} \cdot \boldsymbol{\phi}_c$), where $\boldsymbol{L}$ is the Laplacian operator, and $\boldsymbol{L}^{-1}$ is the inverse Laplacian operator. Then the signals measured by ECoG are written as:

$$\boldsymbol{V}_{ecog} = \boldsymbol{S} \cdot \boldsymbol{L}^{-1} \cdot \boldsymbol{\phi}_c + \boldsymbol{\varepsilon}_{ecog}, \qquad \text{Equation 6}$$

Where $\boldsymbol{S}$ is a selection matrix which picks the voltage on the full cortical grid which are closest to the ECoG electrodes, and $\boldsymbol{\varepsilon}_{ecog}$ is the ECoG sensor noise assumed to be distributed as Gaussian I.I.D. variates. We emphsis that the ECoG Laplacian does not depend at all on the knowledge of the realistic head model or lead field. However, $\boldsymbol{K}_{Lap} = \boldsymbol{S} \cdot \boldsymbol{L}^{-1}$ can be considered as a type of "pseudo lead field", and similar to most inverse problems, Eq. 6 is ill posed, and in order to estimate the Laplacian $\boldsymbol{\phi}_c$, we formulate this problem by penalizing the smoothness of the cortex Laplacian, then the problem can be solved by minimizing the following function:

$$f_{ecog}(\lambda) = \arg\min_{\phi_c} \left\{ \left\| \boldsymbol{V}_{ecog} - \boldsymbol{S} \cdot \boldsymbol{L}^{-1} \cdot \boldsymbol{\phi}_c \right\|_2^2 + \lambda \left\| \boldsymbol{L} \cdot \boldsymbol{\phi}_c \right\|_2^2 \right\} \qquad \text{Equation 7}$$

This is a ridge type regression problem, which minimize the estimations square error as well as penalize the 4th order Laplacian of the cortex voltage, or the 2nd order Laplacian on the cortex. In order to solve the problem defined in Eq. 6 and Eq. 7, we substitute with $\boldsymbol{X} = \boldsymbol{S} \cdot \boldsymbol{L}^{-2}$ and $\boldsymbol{\Phi} = \boldsymbol{L} \cdot \boldsymbol{\phi}_c$. Then, Eq. 7 can be rewritten in the standard ridge regression form as:

$$f_{ecog}(\lambda) = \left\| \boldsymbol{V}_{ecog} - \boldsymbol{X} \cdot \boldsymbol{\Phi} \right\|_2^2 + \lambda \left\| \boldsymbol{\Phi} \right\|_2^2 \qquad \text{Equation 8}$$

Minimizing this function and substitute back, we obtain the estimator for the ECoG Laplacian on the cortical grid:

$$\hat{\boldsymbol{\phi}}_c = \boldsymbol{L}^{-1} \cdot ((\boldsymbol{S} \cdot \boldsymbol{L}^{-2})^T (\boldsymbol{S} \cdot \boldsymbol{L}^{-2}) + \lambda \cdot \boldsymbol{I})^{-1} \cdot (\boldsymbol{S} \cdot \boldsymbol{L}^{-2})^T \cdot \boldsymbol{V}_{ecog} \qquad \text{Equation 9}$$

The hyper parameter λ is selected when the generalized cross validation reaches its minimum. The ECoG Laplacian estimator is calculated for each point of the cortical grid at each time instant, thus also yielding a "cortical grid time series" like the ESI method.

Electrophysiological Source Imaging Methods Submodule

This submodule provdes a uniform interface to the solution of the EECoG inverse problems, and calculate the estimators of current source density $\boldsymbol{J}$. At present, the inverse solutions implemented are listed in Table 1. These methods will not be decribed in detailed here as they are completely specified in the references given and METH toolbox provides the implementations as well. (https://www.uke.de/english/departments-institutes/institutes/neurophysiology-and-pathophysiology/research/working-groups/index.html).

Table 1 The inverse methods implemented in ESI submodule.

Acronym	Name	Reference
MNE	Minimum Norm Estimation	Hämäläinen et al. (1994)
LCMV	Linearly Constrained Minimum Variance Spatial Filtering	Van Veen et al. (1997)
eLORETA	Exact Low Resolution Electromagnetic Tomography	Pascual-Marqui (2007)
SSBL	Sparse Structural Bayesian Learning	Paz-Linares et al. (2017)

In order to compare the source connectivity, we need to be sure that all the ESI methods reached their best performance. For MNE, LCMV and eLORETA, we use the minimum generalized cross validation (GCV) value to select the hyper parameter. For SSBL, the best performance is guaranteed by selecting the hyper paramters when its marginal likelihood function does not increase anymore with iterations.

Each type of inverse solution is calculated for each point on the cortical grid at each time instant. As mentioned before, we need to solve the inverse problem for both EEG and ECoG, then we can compare them on the same source space.

Connectivity Esimation and Comparison Submodules

There are many proposed measures for brain connectivity, both directed and nondirected. We limit our attention of this platform to partial correlations as an undirected brain connectivity measure. This measure has been shown to be less sensitive to indirect connections (Dawson et al. 2016). They can be easily obtained from the inverse of the covariance matrix or precision matrix, which can be normalized to produce the the partial correlation matrix (PCM). There are two specific challenges to be solved for this module:

1. The high dimentionality of the covariance matrices to be studied;
2. The lack of standarized statistical criteria for the selections of significant partial correlations.

We here take advantadge of recently developed theory for inference of high dimensional sparse precision matrices from Jankova et al. (2018) to address these challenges. The assumption of sparsity seems to be natural and widely adopted for estiamtors of brain connectivcity and is relaxed with recent "debiasing" techniques explained below.

The input for the connectivity estimation submodule is the estimated time series at each point of the cortical grid from either ESI methods or the ECoG Laplacian. These time series can be filtered to a specific frequency band of interest, like alpha of 8-12Hz. From these filtered time series, we calculate the empirical covariance matrix. This empirical covaraince matrix is then standardized to produce the emprical correlation matrix $\hat{\mathrm{R}}$. Then, both of them are used to obtain a sparse estimate of the partial correlations, also known as the weighted inverse covarince $\hat{\Theta}_w$ which is estimated by the following minimizing function:

$$f_{\hat{\boldsymbol{\Theta}}_w}(\lambda) = \arg\min_{\boldsymbol{\Theta}=\boldsymbol{\Theta}^T, \boldsymbol{\Theta}\succ 0} \left\{ tr(\hat{\boldsymbol{R}}\boldsymbol{\Theta}) - \log|\boldsymbol{\Theta}| + \lambda \cdot \left\|\boldsymbol{\Theta}^{-}\right\|_1 \right\} \qquad \text{Equation 10}$$

where $\left\|\boldsymbol{\Theta}^{-}\right\|_1$ is the l_1 norm of the off-diagonal elements of the inverse covariance matrix $\boldsymbol{\Theta}$, and λ is the hyper parameter. The computation is readily carried out by the QUIC algorithm (Hsieh et al. 2014), which is one implementation of the graphical LASSO.

We leverage the recent theoretical results from Jankova et al. (2018) in two ways:

First, we can correct the bias introduced by the graphical LASSO with the "debiasing" operation:

$$\hat{\boldsymbol{\Theta}}_c = 2\,\hat{\boldsymbol{\Theta}} - \hat{\boldsymbol{\Theta}}\,\hat{\boldsymbol{\Sigma}}\,\hat{\boldsymbol{\Theta}} \qquad \text{Equation 11}$$

Second, asymptotic normality of the inverse covariances estimator is achieved as stated in Theorem 3 of Jankova's paper (Jankova et al. 2018) with the follwoing transformation:

$$\sqrt{n}\,(\hat{\boldsymbol{\Theta}}_c - \boldsymbol{\Theta}_0)_{ij} / \sigma_{ij} \sim N(0,1), \text{where } \hat{\sigma}_{ij}^2 = \hat{\boldsymbol{\Theta}}_{ii}\hat{\boldsymbol{\Theta}}_{jj} + \hat{\boldsymbol{\Theta}}_{ij}^2\ , \qquad \text{Equation 12}$$

This result allows us to find the thresholds for all the PCMs with the same staistical significance level.

Since we are dealing with very high dimensional PCMs, the threshold must be corrected for multiple comparisons, and it is done by the application of the postive False Discovery Rate $pDFR$ (Storey 2002) as follows:

$$Th(\alpha) = \Phi^{-1}(1 - \frac{pFDR(\alpha)}{2})\,\sigma_{ij} / \sqrt{n} \qquad \text{Equation 13}$$

Finaly, our module compares the thresholded estimated PCMs against a "ground truth" connectivity matrix and give results in terms of ROC curve, which shows the true positive rate (TPR) against false positive rate (FPR) at all possible FPR values.

In order to evaluate the significance of ROC curve, we also calculate the pointwise confidence bound for all the possible FPRs by bootstrap. We correct the the bias introduced from the bootstrap distribution with bias-corrected and accelerated bootstrap interval (BCa interval) method, which is a second-order accurate interval that addresses these problems (Efron 1987; Huang et al. 2007). With this method, we are able to calculate the confidence bands for all the comparisons with significance level 0.05 and number of replicas 200.

The ROC curves allow us to explore the effects of different pFDR choices on the false positive and false negative rates. Since we are only intersted in low FDRs, we summarize the ROC curves with the the partial area under the ROC curve, specificly, we use the standardized partial AUC ($spAUC$) (McClish 1989), which is independ of the level of the specified false positive rate (FPR). It is defined in the following equation, where e is the FPR level we are evaluating:

$$spAUC(e) = \frac{1}{2}\left(1 + \frac{\int_0^e ROC(f)\,df - \frac{e^2}{2}}{e - \frac{e^2}{2}}\right),\ spAUC(e) \in [0,1]. \qquad \text{Equation 14}$$

$spAUC$ varies from 0 to 1, with 0.5 being detection at random and 1 perfect decection.

All the results reported in this paper have been confirmed with bootstrap permutation test ($n = 200$), which shows consistency with very small variances.

5 Source Connectivity Simulation Module: EECoG_scSim

The readers may wonder that, the above 3 modules have almost all the funcitonalities we need to to explore the source level connectivity of the real expeirmental data, why we must provide this source connectivity simulation module? The answer is that, we have many methods to solve the same problem, for example we provide 4 ESI methods plus EcoG Laplacian, but we never know the real "ground truth" beneath the data or which is the most suitable method for our particular data. The only way to answer this question is to create a simulation as similar as possible to the experimental settings. EcoG_scSim is designed to do so by simulate structrued partial correlation matrix as "ground truth" soure level connectivity, and then generate the source activities embeding such connectivity, with the EEG and EcoG lead fields generated from EECoG_FWM, we are able to simulate the same experiemnt with known source connectivity. Together with EECoG_conComp, EECoG-Comp provides tools both for test methods and for exploring data.

EECoG_scSim also provides human based simulation for further validation. A standard human forward model based on the MNI152 template (http://www.bic.mni.mcgill.ca) and standard bioSemi electrodes layouts is calculated with Boundary Element Method (BEM) from BrainStorm (Tadel et al 2011), and the corresponding lead field is provided for human simulation. EECoG_scSim allows the users to change the standard EEG electrode layouts from 10-20 system to 256 electrodes of full head coverage, as well as the size of the cortical grid.

The theory behind this simulation is the same as the forward modeling procedure. The simulated sensor time series $\boldsymbol{V}_{LF}$ for a given head model LF is generated from:

$$\boldsymbol{V}_{LF} = \boldsymbol{K}_{LF}\,\boldsymbol{J}_{\Theta} + \boldsymbol{\varepsilon}_{LF}, \qquad \text{Equation 15}$$

where $\boldsymbol{J}_{\boldsymbol{\Theta}}$ is the current source density sampled independently as $\boldsymbol{J}_{\boldsymbol{\Theta}} \sim N(\boldsymbol{0}, \boldsymbol{\Theta}^{-1})$, with $\boldsymbol{\Theta}$ being the underlying PCM. $\boldsymbol{K}_{LF}$ is the lead field for a given head model. $\boldsymbol{\varepsilon}_{LF}$ is the sensor noise sampled independently from $\boldsymbol{\varepsilon}_{LF} \sim N(\boldsymbol{0}, \boldsymbol{\xi} \cdot \boldsymbol{I})$. The measurement signal to noise ratio (SNR) is 10db for EEG and 20db for ECoG. The length of each cortical grid time series can be the same as the real recordings.

Simulations of $\boldsymbol{J}_{\boldsymbol{\Theta}}$ are based on two different structured PCMs:

1. Sparse random PCM $\boldsymbol{\Theta}_{rand}$, where a small number of the sources on the cortical grids are connected randomly ;
2. Sparse block diagnal PCM $\boldsymbol{\Theta}_{block}$, where a small number of patches of cortical grid points are active and densly connected amongst themselves.

The lead fields used in the simulation module are $\boldsymbol{K}_{H,eeg}$ (Human EEG), $\boldsymbol{K}_{M,eeg}$ (Monkey EEG), $\boldsymbol{K}_{M,ecog}$ (Monkey ECoG) and $\boldsymbol{K}_{Lap}$ (Monkey ECoG Laplaian "pseudo lead field").

6 Open Source and Data Sharing

EECoG-Comp platform is designed with the idea of open source and open data sharing (Poline et al. 2012) and is shared via https://github.com/Vincent-wq/EECoG-Comp, all the results in exploring the MDR data set will be

shared upon request, including the MRI images, the segementation files, the head model files, the lead fields and so on, more details are listed in Table 2.

Tab. 2 Table of shared contents from EECoG-Comp platform.

Folders	Files	Description
1-Nii Images	mcSu_t1[bias corrected]-eq.nii	T1 MRI of the specimen (NIFTI file).
	Svbrain_cSu_t1[bias_corrected].nii	Brain mask.
	Masked_mcSu_t1[bias_corrected]-eq.nii	MRI with non-brain tissue masked out.
2-BrainSuite Segmentations	Csf_Su.nii	Binary cerebrospinal fluid mask.
	Gray_Su.nii	Binary gray matter mask.
	White_Su.nii	Binary white matter mask.
3-SPM Results	c1masked_mcSu_t1[bias corrected]-eq.nii	Probabilistic gray matter mask.
	c2masked_mcSu_t1[bias corrected]-eq.nii	Probabilistic white matter mask.
	c3masked_mcSu_t1[bias corrected]-eq.nii	Probabilistic cerebrospinal fluid mask.
	Masked_mcSu_t1[bias corrected]-eq_seg_inv_sn.mat	Inverse Transformation Template to individual.
	Masked_mcSu_t1[bias corrected]-eq_seg_sn.mat	Transformation from Template to individual.
4-Head Model	EcoG-elecs_Su-silicone_sheet.mat	Surface representing the set of silicone stripes.
	Hybrid3.nii	Image labeling the three head compartments.
	Inskull_Su-corrected.mat	Inner surface of the skull.
	Outskull_Su-corrected.mat	Outer surface of the skull.
	Scalp_Su.mat	Surface of the scalp (MATLAB patch format).
	EcoG-elecs_Su-embbed.mat	ECoG electrodes in the set of silicone stripes.
	EEG-elecs_Su.mat	EEG electrodes on the scalp.
	MESHmodel.2.ele	Elements of the FEM model (generated using TetGen).
	MESHmodel.2.face	Modes of the FEM model (generated using TetGen).
	Cortex-mid_Su.mat	Surface representing cortex.
5-Lead Fields	EcoG-leadfield.mat	Lead field for the EcoG data (MATLAB matrix).
	EEG-leadfield.mat	Lead field for the EEG data.
6-Atlas and Template	c1masked_macaque_25_model-MNI-eq.nii	Gray matter prior for the template.
	c2masked_macaque_25_model-MNI-eq.nii	White matter prior for the template.
	c3masked_macaque_25_model-MNI-eq.nii	Cerebrospinal fluid prior for the template.
	Macaque_25_model-MNI-eq.nii	Template MRI of Macaca Mulatta.
7-Pipelines	EECoG_FWM.zip	The forward model module of EECoG-Comp platform.
	EECoG_Preproc.zip	The preprocess module of EECoG-Comp platform.
	EECoG_scSim.zip	The source connectivity simulation module of EECoG-Comp platform.
	EECoG_conComp.zip	The source connectivity comparison module of EECoG-Comp platform.

3. Results

In this section, we evaluated the performance of different ESI methods in connectivity estimation, specifically in terms of partial correlation matrix (PCM) estimation and took this experiment as an example to illustrate the usage of EECoG-Comp platform. The ESI methods used are MNE, LCMV, eLORETA and SSBL.

We first evaluate the performance of all these methods in EECoG_scSim for both standard human EEG and monkey EECoG simulations (with different number of sources, sensors and PCM structures); Then, we choose the best method from the monkey EECoG simulation as a substitute for "ground truth" to compared against; At last, we use all these ESI methods in exploring the source connectivity in the real data and give the final ranking of all these tested ESI methods as results.

1 Simulations Description

This experiment is started with the generation of structured PCMs of the neural sources (or generators on the cortical mesh), and they are random and block PCMs denoted as $\boldsymbol{\Theta}_{rand}, \boldsymbol{\Theta}_{block}$ (more description in section 2.5). Embeded with these two types of PCMs, the sources activities $\boldsymbol{J}_{\boldsymbol{\Theta}_{rand}}, \boldsymbol{J}_{\boldsymbol{\Theta}_{block}}$ without noise are generated, they are the same as the "ground truth" for all latter simulations. The sensor signals are generated by mulptiplying

the corresponding lead field with the source activities and adding sensor noises, this procedure can be described with the following equations:

$$\boldsymbol{V}_{H,eeg} = \boldsymbol{K}_H \boldsymbol{J}_{(\boldsymbol{\Theta}_{rand},\boldsymbol{\Theta}_{block})} + \boldsymbol{\varepsilon}_{H,eeg}, \quad \text{Equation 16}$$

$$\boldsymbol{V}_{M,eeg} = \boldsymbol{K}_{M,eeg} \boldsymbol{J}_{(\boldsymbol{\Theta}_{rand},\boldsymbol{\Theta}_{block})} + \boldsymbol{\varepsilon}_{M,eeg}, \quad \text{Equation 17}$$

$$\boldsymbol{V}_{M,ecog} = \boldsymbol{K}_{M,ecog} \boldsymbol{J}_{(\boldsymbol{\Theta}_{rand},\boldsymbol{\Theta}_{block})} + \boldsymbol{\varepsilon}_{M,ecog}, \quad \text{Equation 18}$$

$\boldsymbol{V}_{H,eeg}$ is the simulated human sensor EEG with dimension $I_{H,chan} \times I_{tSample}$, $I_{H,chan} \in (19, 32, 64, 128)$ is the number of human EEG channels, and $I_{tSample} = 10800$ is the number of time samples. The sampling frequency is 400Hz for all simulations, these settings are the same as the preprocessed real data. $\boldsymbol{K}_{H,eeg}$ is the Human EEG lead field with dimension $I_{H,chan} \times I_{H,sour}$, $I_{H,chan}$ is the number of human EEG sensors and $I_{H,sour} \in (150, 200, 300, 350)$. $\boldsymbol{\varepsilon}_{H,eeg}$ is the human EEG sensor noise which follows I.I.D. Gaussian distributin $\boldsymbol{\varepsilon}_{H,eeg} \sim \boldsymbol{N(0,\xi \cdot I)}$ with dimension of $I_{H,chan} \times I_{tSample}$. $\boldsymbol{V}_{M,eeg}$ and $\boldsymbol{V}_{M,ecog}$ are generated in the similar way but with monkey EEG lead field $\boldsymbol{K}_{M,eeg}$ ($I_{M,EEG} \times I_{M,sour}$) and monkey ECoG lead field $\boldsymbol{K}_{M,ecog}$ ($I_{M,ECoG} \times I_{M,sour}$). In order to select the best method for the real simultaneous EECoG data, we preserve the same number of the aviliable monkey EEG channels $I_{M,EEG} = 15$ and ECoG chanels $I_{M,ECoG} = 125$, and varying the number of sources $I_{M,sour} \in (150, 200, 300, 350)$, note that, $I_{M,ECoG} < I_{M,\text{sour}}$ and $I_{M,EEG} < I_{M,\text{sour}}$ always hold.

Then, we compare the 4 well-known Electrophysiological Source Imaging (ESI) methods, namely MNE, eLORETA, LCMV and SSBL in human simulation (EEG), and MNE, eLORETA, LCMV and ECoG Laplacian (which is viewed as one of the "pseudo inverse method") in monkey simulations. The source activity estimators for the random source setting are: $\hat{\boldsymbol{J}}_{\boldsymbol{H,eeg,\Theta}_{rand,ESI}}$ (human EEG with different ESI methods) and $\hat{\boldsymbol{J}}_{\boldsymbol{M,eeg,\Theta}_{rand,ESI}}, \hat{\boldsymbol{J}}_{\boldsymbol{M,ecog,\Theta}_{rand,ESI}}$ (monkey EEG and ECoG source activities estimated from different ESI methods), and the source estimators for the block source setting are $\hat{\boldsymbol{J}}_{\boldsymbol{H,eeg,\Theta}_{block,ESI}}$ (human EEG with different ESI methods) and $\hat{\boldsymbol{J}}_{\boldsymbol{M,eeg,\Theta}_{block,ESI}}, \hat{\boldsymbol{J}}_{\boldsymbol{M,ecog,\Theta}_{block,ESI}}$ (monkey EEG and ECoG source activities estimated from different ESI methods). With this simulation, we have both the "ground truth" source activities $\boldsymbol{J}_{\boldsymbol{\Theta}_{rand}}, \boldsymbol{J}_{\boldsymbol{\Theta}_{block}}$ with the "ground truth" source connecitivity $\boldsymbol{\Theta}_{rand}, \boldsymbol{\Theta}_{block}$ as connectivity, and their corresponding estimators from human EEG, monkey EEG and monkey ECoG simulations with different number of sources, different number of sensors and different ESI methods. Before further analysis, we bandpass all the estimated source activation to 8-12Hz and limit the connectivity estimations to alpha band. In order to compare connectivity from different ESI results, we use graphical LASSO (Hsieh et al. 2014) to reconstruct the connectivity estimators ($\hat{\boldsymbol{\Theta}}_{rand}, \hat{\boldsymbol{\Theta}}_{block}$) and compare them with the tools provided by EECoG_conComp. Notice that, for the source activities, we have the "ground truth" $\boldsymbol{J}_{\boldsymbol{\Theta}_{rand}}, \boldsymbol{J}_{\boldsymbol{\Theta}_{block}}$, and we can estimate the source connectivity from them without applying any ESI methods, which is taken as the basic performance to compared against.

Finally, we summaize the simulation results with Performance Improvement Ratio (PIR_{ESI}) of a specific ESI method, which is defined as the improvement ratio of $spAUC(0.1)$ (calculated by comparing $\hat{\boldsymbol{\Theta}}$ against ground truth $\boldsymbol{\Theta}$, see section 2.4 for more details) for a specific ESI method against estimating directly from $\boldsymbol{J}_{\boldsymbol{\Theta}_{rand}}, \boldsymbol{J}_{\boldsymbol{\Theta}_{block}}$, it is formulated as follows:

$$\mathrm{PIR}_{ESI} = \frac{spAUC(0.1)_{ESI} - spAUC(0.1)_{J_\Theta}}{spAUC(0.1)_{J_\Theta}} . \qquad \text{Equation 19}$$

PIR_{ESI} can be positive or negative. Positive PIR_{ESI} indicates that this peticular ESI method even outperforms the direct estimation from the source activities, and vice versa. The whole simulation procedure is illustrated in the flowchart below in Fig.6, and the results will be present in next section.

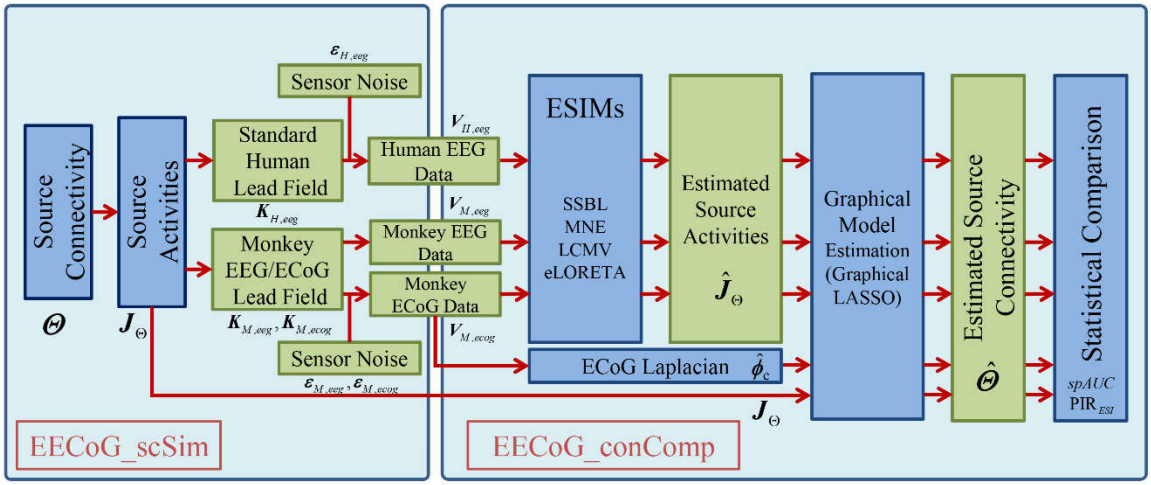

Fig. 6 The flowchart of the ESI methods comparison simulation. Firstly, we use EECoG_scSim to generate human EEG simulation $\boldsymbol{V}_{H,eeg}$ and monkey EECoG simulations $\boldsymbol{V}_{M,eeg}$ and $\boldsymbol{V}_{M,ecog}$ with two types of known structured source connectivity ($\boldsymbol{\Theta}_{rand}, \boldsymbol{\Theta}_{block}$) and source activities ($\boldsymbol{J}_{\boldsymbol{\Theta}_{rand}}, \boldsymbol{J}_{\boldsymbol{\Theta}_{block}}$); Secondly, we use EECoG_conComp to compare the ESI methods and estimate the underlying connectivity in terms of partial correlation matrix; Thirdly, compare the connectivity estimators from different ESI methods against that estimated from the "ground truth" source activity, and find the method with the highest PIR_{ESI} as the best method; Last but not least, we use this method as a substitute for "ground truth" for latter real data exploration and ESI methods comparison in section 3.3.

2 Comparison of ESI methods applied to the Simulations

In this section, we present the results from human EEG and monkey EECoG simulations.

Human EEG Simulation

In the human simulation, we are testing the performance of different ESI methods on the standard human headmodel (MNI152 template http://www.bic.mni.mcgill.ca) with different electrode layouts and different sizes of cortical grids. In this simulation, the number of sensors is $I_{chan} \in (19, 32, 64, 128)$ for 10-20 system, 32,64, and 128 channel system with whole head coverage, the number of sources is $I_{sour} \in (150, 200, 300, 350)$ over the whole cortex. Due to the computational load of graphical model estimation and ROC evaluation (bootstrapping for ROC confidence band), we are only simulating small cortical grids, therefore we have 16 results in total (4 number of senors times 4 grid sizes) for each type of source connectivity setting.

The results are summarized in Fig. 7, it shows the ESI methods performance improvements in terms of PIR_{ESI} for both random and block sources for various sensor and source configurations. In summary, PIR_{ESI} of all the ESI methods did not show improvements larger than 10%. To be specific, for random source as in Fig.7(a), almost all of the ESI methods are giving negative PIR_{ESI}, which means they are worse than the direct estimation from the source activity. For the block strtuctured source (which toughed to be closer to the real case), LCMV, eLORETA and SSBL show limited improvements, but no better than 10%, while MNE is still giving negative results in most configurations. Varying the number of sensors and sources does not show clear partterns.

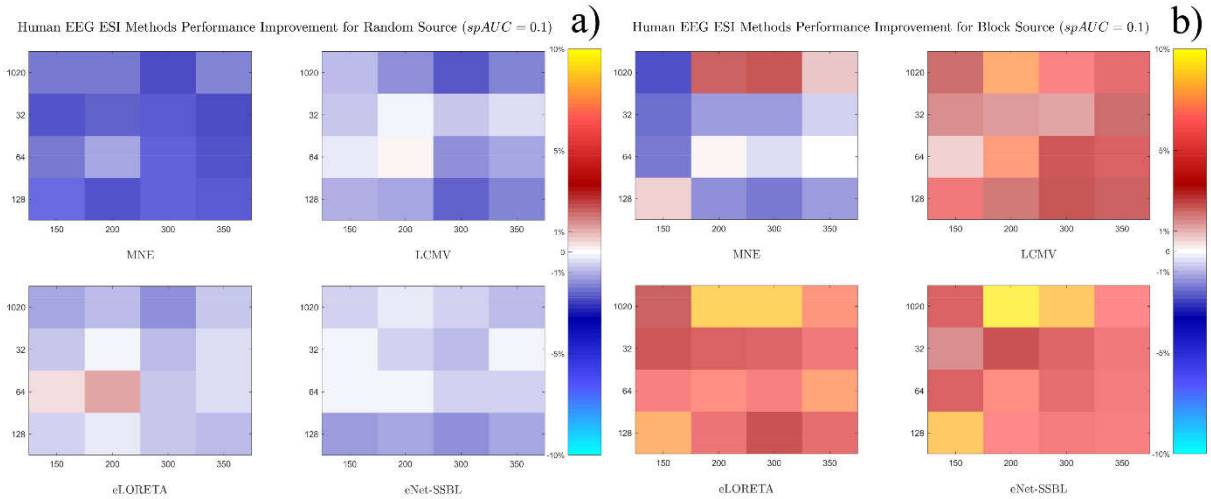

Fig. 7 The PIR_{ESI} of ESI methods from human simulation for: a) random structured source PCM (left), and b) block structured diagonal source PCM (right). Each color matrix in the subfigures summarize the results from one specific ESI method with different number of sensors and sources, and they are: MNE (upper left), LCMV (upper right), eLORETA (lower left), and elastic net SSBL (lower right). In each matrix, results from different configurations are presented: the row denotes different EEG electrode layouts: 1020 system, 32 Channel, 64 Channel and 128Channel (top to bottom), and the column represents number of sources: 150, 200, 300, 350 (left to right). **The color encoding is rescaled to [-10%, 10%]** for better illustration.

Simultaneous Monkey EECoG Simulation

EECoG-Comp platform allows us to simulate simultaneous monkey EECoG data to test not only the ESI methods but also ECoG Laplacian described in Section 2.4. Due to the fixed number of EECoG channels in the real experiment, we only tested the performance of ESI methods across different sizes of cortical grids: $I_{sour} \in (150, 200, 300, 350)$, the methods tested in this simulation are MNE, LCMV, eLORETA and ECoG Laplacian. This means for each data (EEG or ECoG), we have 4 groups of results for each type of structured source connectivity.

The results from this simulation are summarized in Fig. 8, and they show accordance with the human EEG simulation. For the random PCM source in Fig. 8(a), all the ESI methods are giving negative PIR_{ESI} s, which means all the methods did not improve the source connectivity estimatation compared with direct estimation from the source activity. ECoG does not outperforms EEG either, averagely ECoG Laplacian provides the least bad results, and the performance is better when the cortical grid has more vertices. It is totally different for the block source connectivity as shown in Fig. 8(b), except EEG and ECoG with 150 sources, some of the ESI methods give positive values, and ECoG Laplacian always has the largest improvement.

In total, the improvements and drawbacks present in this monkey simulation are within 5%, and by now, ECoG Laplacian improves the source connectivity estimation the most, thus is though to be the best “ESI method” for this MDR data set.

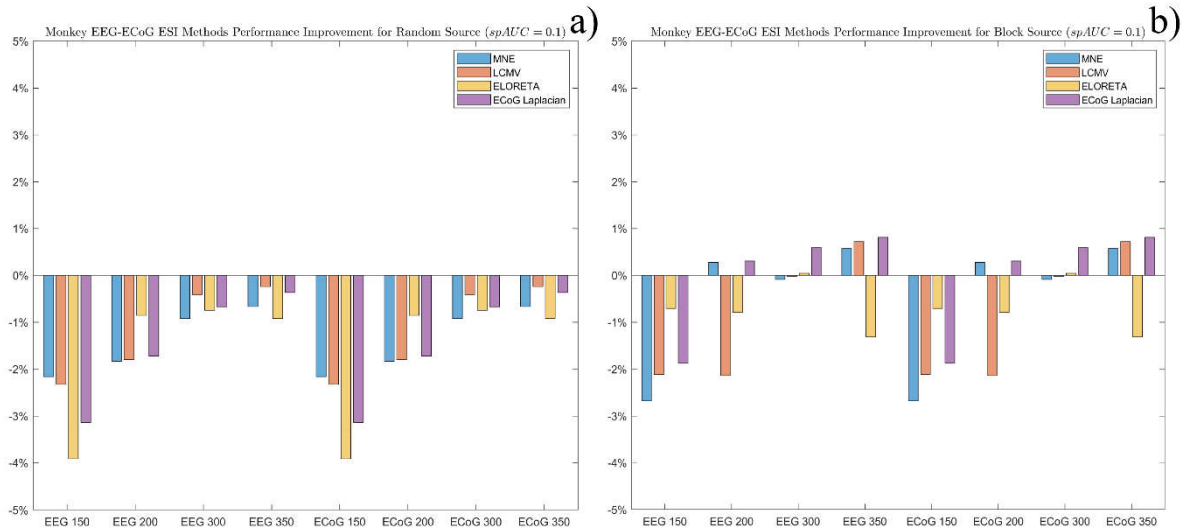

Fig. 8 The PIR_{ESI} of ESI methods from monkey EECoG simulations for: a) random structured source PCM (left), and b) block structured diagonal source PCM (right). Each bar stands for one ESI method: MNE (blue), LCMV (orange), eLORETA (yellow), and ECoG Laplacian (purple). Each cluster of bars represents a group of simulation with the saming head model. From left to right, they are the first 4 groups of EEG with number of sources 150, 200, 300, and 350, and 4 groups of ECoG with the same number of source. The **y axis is rescaled to [-5%, 5%] (different from Fig. 7)** for better illustration.

3 ESI methods Comparison with the Real Simultaneous EECoG MDR Data

Even though the ECoG Laplacian connectivity estimatation did not yield huge performance improvement in the simulations, it did provide the highest PIR_{ESI}. Therefore, we choose the ECoG Laplacian as a substitute for the "ground truth" when exploring the real data and compare the ESI methods against ECoG Laplacian.

In the MDR data analysis, we first cleaned the data with EECoG_Preproc, then input the data to EECoG_conComp. By applying different ESI methods, we estimated the source activities and ECoG Laplacian, bandpassed to alpha band (8-12 Hz), estimated the graphical model parameters with graphical LASSO and do the statistical evaluation of the similarity between the ESI reconstructed partial correlation matrix (PCM) and ECoG Laplacian PCM. The results are summarized in the bar diagram below in Fig. 9 in terms of $spAUC(0.1)$.

All the results give comparatively higher $spAUC(0.1)$ values ($spAUC_{0.1} \in [0.6127 \sim 0.7362]$ with mean 0.6496 and standard deviation 0.0474, $spAUC(0.1)$ is less than 0.6 for human simulation and less than 0.52 for monkey simulation, slightly better than random guessing), showing that all the methods are giving similar results to the connectivity obtained from the ECoG Laplacian.

It is also interesting to see that all the methods are giving "higher $spAUC$ for the awake state data, and ECoG outperforms EEG more than 10%. On the contrary, in anesthesia state, all the methods give equally low accuracy compared with ECoG Laplacian, there is even no clear performance difference bewteen EEG and ECoG in the anesthesia state data.

As to the performance of the 4 different ESI methods (taking ECoG Laplacian as a standard), their performance differences are very small (less than 5%). If we rank them, eLORETA is always in the first place, and their ranks vary for different datasets: 1) EEG awake (always in performance decreasing order): eLORETA>MNE> LCMV>eNet-SSBL; 2) ECoG awake: eLORETA>LCMV>eNet-SSBL>MNE; 3) EEG anesthesia: eLORETA>MNE>eNet-SSBL>LCMV; 4) ECoG anesthesia: eLORETA>MNE>eNet-SSBL>LCMV. The overall rank is eLORETA>MNE>eNet-SSBL=LCMV. Notice that, the ranks are the same in anesthesia state data for both EEG and ECoG, but very different for EEG and ECoG in the awake state data.

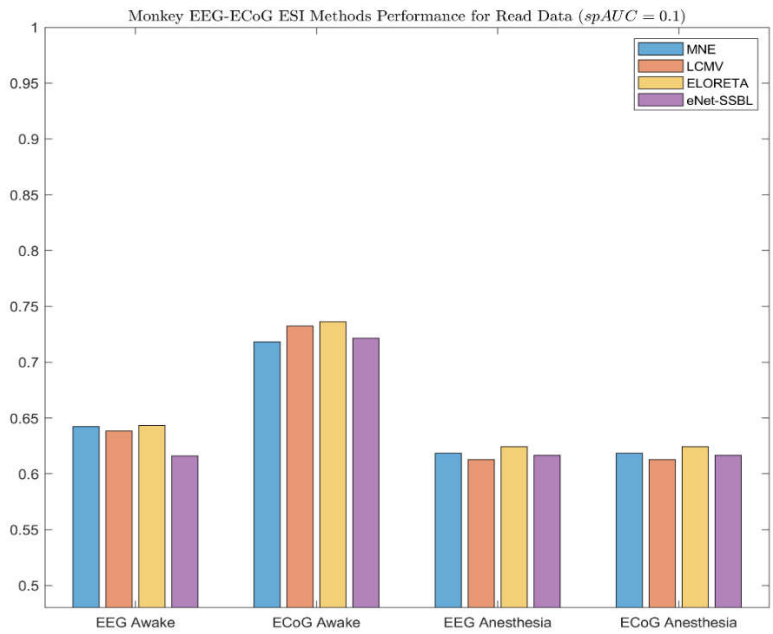

Fig. 9 The $spAUC(0.1)$ of ESI methods performance in simultaneous EECoG real data. Each bar stands for one ESI method: MNE (blue), LCMV (orange), eLORETA (yellow) and elastic-net SSBL (purple). Each cluster of bars represents a group of recordings: they are EEG awake, ECoG Awake, EEG Anesthesia and ECoG Anesthesia (from left to right). **The y axis is rescaled to [0.5, 1] for better comparison, notice that, this scale is different from all the previous figures.**

4. Discussion

In this paper, we provide EECoG-Comp, an open source EEG and ECoG comparison platform, and illustrate its use with a particular simultaneous EEG and ECoG data set. The modular design of this platform allows us to evaluate the performance of any individual component in analyzing EECoG data, like ESI methods submodule, from the whole platform with comparison in both (standard and customized) simulations and real data. We take source connectivity estimation comparison form 4 popular ESI methods (MNE, eLORETA, LCMV and SSBL) with the MDR data set as a task to illustrate the use of this EECoG-Comp platform, and this platform can give both theoretical comparison results from standard human simulation and customized simultaneous monkey EECoG simulations (as in the real MDR data) and the comparison results from the real MDR EECoG data with equivalent statistical significance level. We discuss the features of this EECoG-Comp platform revealed by the detailed analysis of the MDR data set.

One striking feature of this particular data set revealed by the EECoG-Comp platform was the absence of alpha activity. Careful artifact control and signal processing procedures failed to show a spectral peak in the alpha range. This may be due to the circumstances of the recording in which the monkey was blindfolded but may have been very alert due to unrolled factors.

Use of the simulation and source connectivity comparison modules from EECoG-Comp platform allowed the comparison of connectivity estimation from different ESI methods. Several preliminary conclusions emerge:

1. The results from this paper shows accordance with several other papers (Mahjoory et al. 2017; Palva et al. 2018) that most ESI methods suffer from very high level of false positive and false negative connections.
2. Sparse random source connectivity estimation is still challenging, almost none of the ESI methods or ECoG Laplacian is able to improve the accruracy of source connectivity reconstruction compared with direct estimation from the sources activities.
3. There is an improvement in performance for source connectivity estimation that have a “block” type of activations and partial correlations, which may be less sensitive to the effects of “leakage” (Paz-Linares et al. 2018). This is consistent with the results described by Todaro (2018) which quantified the effect of

leakage for this same preparation. The accuracy of ESI methods is still very low, even though significantly different from chance level and has improvements over direct estimation from the source activities.

4. The ECoG Laplacian (Nunez and Srinivasan 2006), which does not depend on the solution of the forward modeling, is slightly better in performance than the ESI connectivity estimators. But it still does not provide high accuracy. We believe that, this result points to the need for both better forward models (Piastra et al. 2018) as well as better methods to deal specifically with accuracy of source connectivity estimations (Palva et al. 2018; Gonzalez-Moreira et al. 2018).
5. Despite the similar performances of ESI methods in both simulations and MDR data analysis, their performances in random structured source simulation and in the anesthesia data show accordance, and so do their performances in the block structured source simulations and in the awake data. All the ESI methods including ECoG Laplacian performs similarly poor in the anesthesia state and in the random source simulations. They perform better and the performance differences grow larger in the block source simulations and awake state data. This may provide a support for the organized brain connectivity structure of the consciousness brain state.
6. Since the best achievable accuracy in simulations was from the ECoG Laplacian, and the ESI connectivity estimators evaluated performed similarly to the ECoG Laplacian. We suggest that this might indicate that the ECoG might not be the best tool to investigate the actual primary current density, that future experiments might need Local Field Potential measurements (Bimbi et al. 2018). Current technological advances may enable this type of wide coverage joint EEG-LFP experiment soon.

Use of this EECoG-Comp platform on the MDR data set may also guide the design of future protocols. For example:

1) We have shown that the removed EEG channels are all close to the ECoG connector, and only 15 EEG channels left, which is very challenging for all the inverse estimations, thus we may suggest a higher density recording system like 32 channel EEG, but not that high as 128 channels due to the evaluation in simulations.
2) The subject is a male monkey, who has very thick muscles on both sides of head (see Fig. 5), which not only makes the forward modeling more difficult (may need to model the muscle as another independent counterpart with different electrical properties) but also introduces more artifacts, thus we may suggest to choose a female subject for the similar experiments.
3) We have witnessed that none of the ESI methods works well in exploring the anesthesia brain even in simulation for both EEG and ECoG, which means we'd better add more task sessions for latter experiments if ESI methods evaluation is the purpose of future research.
4) The data gathered from the improved protocols may also be easily analyzed with this EECoG-Comp platform.

Thus, the analysis of the MDR data set with this EECoG-Comp platform cannot only compare different ESI methods in both simualtions and real data, but also provide suggestions for future experiments. We share this platform via https://github.com/Vincent-wq/EECoG-Comp so that ESI researchers can access, extend and customize it for their own EECoG analysis.

5. Conclusion

In this paper, we first provide the open source EECoG-Comp platform, which aims to help the researchers analyize the source level connectivity of simultaneous EEG and ECoG experimental data, to achive this goal, this platform offers four modules: 1) EECoG_Preproc to clean the recordings and reject artifacts, 2)EECoG_FWM to build the realistic biophysical forward model for EEG and ECoG, 3) EECoG_conComp for inverse solutions, connectivity estimation, and statistical comparison, and 4) EECoG_scSim for source level connectivity simulation and server as the null model for self validation and exploring the real data. This platform has great potential in solving the following problems: 1) evaluate the effectiveness of EEG analytical methods (compare to ECoG), 2) evaluate different ESI methods (the example we use to demonstrate the usage of this platform), 3) evaluate different connectivity estimators. In order to demonstrate the application of this platform, we take the simultaneous EEG/ECoG data of a *macaca fuscata* from neurotycho.org as an example, build the head model with FEM, clean the data, and test different ESI methods in both simulations and real data.

The results of this example not only show that none of the tested ESI methods is able to give accurate source connectivity reconstructions in terms of source partial correlation matrix, but also provide practical suggestions for the future protocols. In summary, this platform is able to help the researchers to explore this type of simultaneous EEG and ECoG data and get more reliable and confident conclusions.

Acknowledgements and Author Contributions

The authors would like to thank the helpful discussions with Carsten Wolters, Marios Antonakakis, Maria Carla Piastra, and Laura Marzetti in forward modeling, the discussions with Prof. Peng Ren, Mayrim Vega Hernandez , and Eduardo Martinez Montes with simulation and inverse solutions, and thanks Shiang Hu with the help in reference selection and spectrum decomposition. The authors also would like to thank for the support from the Tri-national axis in normal and pathological cognitive aging project with No. 81861128001, and the funds from National Nature and Science Foundation of China (NSFC) with funding No. 61871105, 61673090, and 81330032, and CNS Programme of UESTC with No. Y03111023901014005.

References

Bassett DS, Sporns O (2017) Network neuroscience. Nature Neuroscience 20(3):353

Buxhoeveden DP, Casanova MF (2002) The minicolumn hypothesis in neuroscience. Brain 125(5):935-51

Bokil H, Andrews P, Kulkarni JE, Mehta S, Mitra PP (2010) Chronux: a platform for analyzing neural signals. Journal of Neuroscience Methods 192(1):146–151

Delorme A, Scott M (2004) EEGLAB: an open source toolbox for analysis of single-trial EEG dynamics including independent component analysis. Journal of Neuroscience Methods 134(1): 9-21

Ding L, Wilke C, Xu B, Xu X, van Drongelene W, Kohrman M, He B (2007) EEG source imaging: correlate source locations and extents with ECoG and surgical resections in epilepsy patients. Journal of Clinical Neurophysiology: official publication of the American Electroencephalographic Society 24(2):130

Efron B (1987) Better bootstrap confidence intervals. Journal of the American Statistical Association 82(397):171-185

Frauscher B, von Ellenrieder N, Zelmann R, et al. (2018) Atlas of the normal intracranial electroencephalogram: neurophysiological awake activity in different cortical areas. Brain 141(4): 1130-1144

Gonzalez-Moreira E, Paz-Linares D, Martinez-Montes E, Valdes-Hernandez P, Bosch-Bayard J, Bringas-Vega ML, Valdes-Sosa P (2018) Populational Super-Resolution Sparse M/EEG Sources and Connectivity Estimation. bioRxiv. https://www.biorxiv.org/content/10.1101/346569v1

Grech R, Cassar T et al. (2008) Review on solving the inverse problem in EEG source analysis. Journal of Neuroengineering and Rehabilitation 5(1):25

He B, Yang L, Wilke C, Yuan H (2011) Electrophysiological imaging of brain activity and connectivity—challenges and opportunities. IEEE Transactions on Biomedical Engineering 58(7):1918-31

Hsieh CJ, Sustik MA, Dhillon IS, Ravikumar P (2014) QUIC: quadratic approximation for sparse inverse covariance estimation. The Journal of Machine Learning Research 15(1):2911-47

Hallez H, Vanrumste B, Grech R, Muscat J, De Clercq W, Vergult A, Asseler AD, Camilleri KP, Fabri SG, Van Huffel S et al. (2007) Review on solving the forward problem in EEG source analysis. Journal of Neuroengineering and Rehabilitation 4(1):46

Hämäläinen MS, Ilmoniemi RJ (1994) Interpreting magnetic fields of the brain: minimum norm estimates. Medical Biological Engineering Computing 32(1):35–42

Huang Y, Sullivan Pepe M, Feng Z (2007) Evaluating the predictiveness of a continuous marker. Biometrics 63(4): 1181-1188

Jankova J, van de Geer S (2018) Inference in high-dimensional graphical models. arXiv. https://arxiv.org/abs/1801.08512

Friston KJ (2011) Functional and effective connectivity: a review. Brain Connectivity 1(1):13–36

Leahy RM, Mosher JC et al. (1998) A study of dipole localization accuracy for MEG and EEG using a human skull phantom. Electroencephalography and Clinical Neurophysiology 107(2): 159-173

Marin G, Guerin C, Baillet S, et al. (1998) Influence of skull anisotropy for the forward and inverse problem in EEG: simulation studies using FEM on realistic head models. Human Brain Mapping, 6(4): 250-269

Mahjoory K, Nikulin VV, Botrel L, Linkenkaer-Hansen K, Fato MM, Haufe S (2017) Consistency of EEG source localization and connectivity estimates. Neuroimage 152:590–601

Mattia M, Ferraina S, Del Giudice P. (2010) Dissociated multi-unit activity and local field potentials: a theory inspired analysis of a motor decision task. Neuroimage 52(3): 812-823

McClish DK (1989) Analyzing a portion of the ROC curve. Medical Decision Making 9(3):190-5

Nunez PL, Nunez MD, Srinivasan R (2019) Multi-Scale Neural Sources of EEG: Genuine, Equivalent, and Representative. A Tutorial Review. Brain Topography 1-22

Nagasaka Y, Shimoda K, Fujii N (2011) Multidimensional recording (MDR) and data sharing: an ecological open research and educational platform for neuroscience. PLoS ONE 6(7): e22561

Oosugi N, Kitajo K, Hasegawa N, Nagasaka Y, Okanoya K, Fujii N (2017) A new method for quantifying the performance of EEG blind source separation algorithms by referencing a simultaneously recorded ECoG signal. Neural Networks 93:1-6

Oosugi N, Kitajo K, Hasegawa N, Nagasaka Y, Okanoya K, Fujii N(2017) A new method for quantifying the performance of EEG blind source separation algorithms by referencing a simultaneously recorded ECoG signal. Neural Networks 93:1–6

Oostenveld R, Fries P, Maris E, Schoffelen JM (2011) FieldTrip: open source software for advanced analysis of MEG, EEG, and invasive electrophysiological data. Computational Intelligence and Neuroscience 1

Paz-Linares D et al. (2018) Caulking the Leakage Effect in MEEG Source Connectivity Analysis. ArXiv. https://arxiv.org/abs/1810.00786

Paz-Linares D, Vega-Hernandez M, Rojas-Lopez PA, Valdes-Hernandez PA, Martinez-Montes E, Valdes-Sosa PA (2017) Spatio temporal EEG source imaging with the hierarchical Bayesian elastic net and elitist LASSO models. Front. Neurosci. 11:635

Poline JB, Breeze JL, Ghosh SS, Gorgolewski K, Halchenko YO, Hanke M, Ashburner J (2012) Data sharing in neuroimaging research. Frontiers in Neuroinformatics 6:1-9

Papadopoulou M, Friston KJ, Marinazzo D (2015) Estimating directed connectivity from cortical recordings and reconstructed sources. Brain Topography https://doi.org/10.1007/s10548-015-0450-6

Piastra MC, Nüßing A, Vorwerk J, Bornfleth H, Oostenveld R, Engwer C, Wolters CH (2018) The Discontinuous Galerkin Finite Element Method for Solving the MEG and the Combined MEG/EEG Forward Problem. Frontiers in Neuroscience 12:30

Pascual-Marqui RD (1999) Review of methods for solving the EEG inverse problem. International Journal of Bioelectromagnetism 1(1):75–86

Pascual-Marqui RD (2007) Discrete, 3d distributed, linear imaging methods of electric neuronal activity. part 1: exact, zero error localization. arXiv. https://arxiv.org/abs/0710.3341

Simbio Consortium (2000) Simbio: A generic environment for bio-numerical simulation

Schomer DL, Da Silva FL (2012) Niedermeyer's electroencephalography: basic principles, clinical applications, and related fields. Lippincott Williams & Wilkins

Shattuck DW, Sandor-Leahy SR, Schaper KA, Rottenberg DA, Leahy RM (2001) Magnetic resonance image tissue classification using a partial volume model. NeuroImage 13(5):856–876

Shattuck DW, Leahy RM (2002) BrainSuite: an automated cortical surface identification tool. Medical Image Analysis 6(2):129-142

Si H (2015) TetGen, a Delaunay-based quality tetrahedral mesh generator. ACM Transactions on Mathematical Software (TOMS) 41(2):11

Selesnick IW, Graber HL, Ding Y, Zhang T, Barbour RL (2014) Transient artifact reduction algorithm (TARA) based on sparse optimization. IEEE Transactions on Signal Processing 62(24):6596–6611

Storey JD (2002) A direct approach to false discovery rates. Journal of the Royal Statistical Society: Series B 64(3):479-98

Todaro C, Marzetti L, Valdés-Sosa PA, Valdés-Hernandez PA, Pizzella V (2018) Mapping Brain Activity with Electrocorticography: Resolution Properties and Robustness of Inverse Solutions. Brain Topography 1:16

Tadel F, Baillet S, Mosher JC, Pantazis D, Leahy RM (2011) Brainstorm: a user-friendly application for MEG/EEG analysis. Computational Intelligence and Neuroscience 1:8

van den Broek SP, Reinders F, Donderwinkel M, Peters M (1998) Volume conduction effects in EEG and MEG. Electroencephalography and Clinical Neurophysiology 106(6):522–534

Wang X, Pang Y, Ku G, et al. (2003) Noninvasive laser-induced photoacoustic tomography for structural and functional in vivo imaging of the brain. Nature Biotechnology 21(7): 803

Xia M, Wang J, and He Y (2013) Brainnet viewer: a network visualization tool for human brain connectomics. PLoS ONE 8(7): e68910

Xanthopoulos P, Sakkalis V, Vanrumste B (2008) Review on solving the inverse problem in EEG source analysis. Journal of Neuroengineering and Rehabilitation 5(1):25

Zalesky A, Fornito A, Bullmore ET (2010) Network-based statistic: identifying differences in brain networks. Neuroimage 53(4):1197-1207

Appendix

Table 3: Notations for variables and functions

Basic Mathematical Notations			
Item	Variable	Definition	
1.1	$x \in \mathbb{R}$	Variable.	
1.2	$\boldsymbol{x} \in \mathbb{R}^N$	Vector.	
1.3	$\boldsymbol{X}^{I_1 \times I_2}$, $X^{I_1 \times I_2} \in \mathbb{R}^{I_1 \times I_2}$	Matrix (bold capital) and matrix operator (normal capital) with dimensions of $I_1 \times I_2$.	
1.4	I_{chan}, I_{sour}, $I_{tSample}$	The dimension of EEG, leadfield, and source matrices, to be specific, I_{chan} is the number of channels, I_{sour} is the number of sources and $I_{tSample}$ is the number of time samples.	
1.5	$\boldsymbol{X}, \boldsymbol{X}^{-1}, \boldsymbol{X}^T, \boldsymbol{X}^-$	Matrix, its inverse, its transpose and its off-diagonal elements.	
1.6	$\log(\boldsymbol{X}), \Phi^{-1}(\alpha)$	Natural logarithm of a matrix and the inverse cumulation density function for standard normal distribution at $\mathrm{Prob} = \alpha$.	
Concepts and Variables			
Item	Variable	Definition	First Appear

2.1	$\boldsymbol{v}_{ob}$	Vector, general observed EEG signal, $\boldsymbol{v}_{ob} \in \mathbb{R}^N$.	Section 3.1
2.2	$\boldsymbol{a}_1, \boldsymbol{a}_2$	Vectors, type 1 and type 2 artifacts, which model the sparse spike artifact and sparse step like artifact, respectively, $a_1, a_2 \in \mathbb{R}^N$	Section 3.1
2.3	$\boldsymbol{v}_c$	Vector, type1 and type2 artifacts free signal (Low pass) after TARA artifact removal of $\boldsymbol{v}_{ob}$, $\boldsymbol{v}_c \in \mathbb{R}^N$.	
2.4	$\boldsymbol{\mu}$	Vector, additive Gaussian white noise, $\boldsymbol{\mu} \sim N(0,1)$.	Section 3.1
2.5	$\boldsymbol{V}_{eeg}$, $\boldsymbol{V}_{ecog}$, $\boldsymbol{V}_{LF}, \boldsymbol{V}_{cortex}$	Matrices with dimension $I_{chan} \times I_{tSample}$ (number of channels by number of time samples). They are measured EEG, ECoG signals from the available channels, the simulation signals from a specific head model LF (refer to 2.9 in this table) and the voltages on the cortex with dimensions $I_{sour} \times I_{tSample}$.	Section 3.2, Section 3.3, Section 3.6
2.6	$\boldsymbol{K}_{eeg}$, $\boldsymbol{K}_{ecog}$, $\boldsymbol{K}_{LF}, \boldsymbol{K}_{Lap}$	Matrices with dimension $I_{chan} \times I_{sour}$ (number of channels by number of sources). $\boldsymbol{K}_{eeg}$, $\boldsymbol{K}_{ecog}$, $\boldsymbol{K}_{LF}$ are leadfields for EEG, ECoG, and the leadfield used in simulation from a specific head model LF (refer to 2.9 in this table). $\boldsymbol{K}_{Lap}$ is the "pseudo leadfield" for monkey ECoG Laplacian.	Section 3.2, Section 3.3, Section 3.6
2.7	$\boldsymbol{J}, \boldsymbol{J}_{\Theta}, \hat{\boldsymbol{J}}_{\Theta}$,	Matrices with dimension $I_{sour} \times I_{tSample}$ (number of sources by number of time samples). The primary current density, the primary current density with underlying partial correlation matrix (PCM) $\boldsymbol{\Theta}$, and $\boldsymbol{J}_{\Theta} \sim \boldsymbol{N}(\boldsymbol{0}, \boldsymbol{\Theta}^{-1})$ (refer to 2.13 in this table) and its estimator.	Section 3.2, Section 3.6
2.8	$\boldsymbol{\varepsilon}_{eeg}, \boldsymbol{\varepsilon}_{ecog}$, $\boldsymbol{\varepsilon}_{LF}$	Matrices with dimension $I_{chan} \times I_{tSample}$ (number of channels by number of time samples). The additive sensor noise for EEG, ECoG, and a specific head model LF (refer to 2.9 in this table), $\boldsymbol{\varepsilon}_{LF} \sim \boldsymbol{N}(\boldsymbol{0}, \xi ? \boldsymbol{I})$.	Section 3.2, Section 3.6
2.9	LF	The detailed configuration of a head model (M for macaque and H for human), for example: $\boldsymbol{K}_{M,ecog}$ denotes the leadfield for macaque ECoG, dimension of the corresponding leadfield is $I_{chan} \times I_{sour}$ (number of channels by number of sources).	Section 3.2
2.10	$\boldsymbol{S}$	Selection matrix ($I_{chanECoG} \times I_{sour}$,number of ECoG channels by number of sources) for picking the voltage on the full cortical grid, which are closest to the ECoG electrodes.	Section 3.3
2.11	$\boldsymbol{L}, \boldsymbol{L}^{-1}$	Laplacian operator ($I_{sour} \times I_{sour}$, number of sources by number of sources) over the cortical grid, and the inverse Laplacian operator over the cortical grid.	Section 3.3

2.12	$\boldsymbol{\phi}_{\mathrm{c}}$, $\hat{\boldsymbol{\phi}}_{\mathrm{c}}$	ECoG Laplacian, and the estimated ECoG Laplacian on the cortical grid ($I_{sour} \times I_{tSample}$, number of sources by number of time samples).	Section 3.3
2.13	$\hat{\boldsymbol{\Theta}}_w, \boldsymbol{\Theta}_{rand}$, $\boldsymbol{\Theta}_{block}$	PCMs with dimension $I_{sour} \times I_{sour}$ (number of sources by number of sources). They are the estimated PCM, the simulated random PCM, and the simulated block PCM.	Section 3.5, Section 3.6
2.14	$\hat{\boldsymbol{\Sigma}}$	The empirical covariance with dimension $I_{sour} \times I_{sour}$ (number of sources by number of sources) as an estimator for the underlying covariance matrix.	Section 3.5,
2.15	$\hat{\boldsymbol{R}}$	The empirical correlation matrix with dimension $I_{sour} \times I_{sour}$ (number of sources by number of sources) as an estimator for the underlying correlation matrix, $\hat{\boldsymbol{R}}$ is the normalized version or weighed $\hat{\boldsymbol{\Sigma}}$.	Section 3.5,
2.16	$\hat{\boldsymbol{\Theta}}_c$	The de-biased PCM with dimension $I_{sour} \times I_{sour}$ (number of sources by number of sources), and the bias introduced by graphical LASSO removed.	Section 3.5,
2.17	$\hat{\sigma}_{ij}^2$	A variance estimator in the elementwise statistical test $\sqrt{n}\,(\hat{\boldsymbol{\Theta}}_c - \boldsymbol{\Theta}_0)_{ij} / \sigma_{ij} \sim N(0,1)$, where $\boldsymbol{\Theta}_0$ is the null hypothesis, which states the nonexistence of any connections in the source PCM ($\boldsymbol{\Theta}_0 = \boldsymbol{0}^{sour \times sour}$ has the same dimension as $\hat{\boldsymbol{\Theta}}_c$), refer to Jankova et al. (2018) for more details.	Section 3.5,
Operators and Functions			
Item	Operator and Function	Definition	First Appear
3.1	A	Low pass filter.	Eq. 3 in Section 3.1
3.2	B	High pass filter, $B = \boldsymbol{I} - A$.	Eq. 2 in Section 3.1
3.3	D	First order differential operator.	Eq. 13 in Section 3.5
3.4	$f_{a_1,a_2}(\lambda_0, \lambda_1, \lambda_2)$	Optimization function for TARA (Selesnick et al. 2014), λ_i is the regularization parameter, $\lambda_i \in \mathbb{R}^N$.	Eq. 2 in Section 3.1
3.5	ψ_0, ψ_1, ψ_2	Penalty functions for $f_{a_1,a_2}(\lambda_0, \lambda_1, \lambda_2)$, they can be l_1 or l_2 norm.	Eq. 2 in Section 3.1
3.6	$f_{ecog}(\lambda)$	Optimization function for estimating the cortical Laplacian $\hat{\boldsymbol{\phi}}_{\mathrm{c}}$, where λ is the regularization parameter, $\lambda_i \in \mathbb{R}^N$.	Eq. 7 in Section 3.3
3.7	$f_{\hat{\boldsymbol{\Theta}}_w}(\lambda)$	Optimization function for graphical LASSO to estimate $\hat{\boldsymbol{\Theta}}_w$ (Jankova et al. 2018), where λ is the regularization parameter, $\lambda \in \mathbb{R}^N$.	Eq. 10 in Section 3.5
3.8	$pDFR(\alpha)$	Positive FDR introduced by Storey (2002).	Eq. 13 in Section 3.5
3.9	$Th(\alpha)$	Threshold obtained from Eq.13 with certain significance level α corrected by positive FDR (Storey 2002).	Section 3.5,

3.10	$spAUC(e)$ or $spAUC_e$	Standard partial area under curve with false positive rate of e introduced by McClish (1989).	Eq. 14 in Section 3.5
3.11	PIR_{ESI}	Performance Increase Ratio for a specific ESI method.	Eq. 19 in Section 4.1